ChemComm

COMMUNICATION

View Article Online
View Journal

Cite this: DOI: 10.1039/d5cc06807j

Received 30th November 2025,
Accepted 5th February 2026

DOI: 10.1039/d5cc06807j

rsc.li/chemcomm

A highly active and durable bimetallic $CoMnO_x$ catalyst supported on carbon nanofibers for peroxymonosulfate activation toward water treatment

Siyu Ren, Yue Zhang, Linfeng Zhang and Xiaofeng Lu *

A bimetallic $CoMnO_x$ catalyst supported on carbon nanofibers has been constructed for peroxymonosulfate (PMS) activation.

In contemporary water treatment technologies, the effective and targeted elimination of hazardous contaminants is substantially challenging.[1] In recent years, peroxymonosulfate (PMS)-activated oxidation systems have emerged as a prominent research focus in advanced oxidation processes (AOPs), demonstrating remarkable potential for environmental remediation.[2,3] Reactive oxygen species (ROS), including free radicals like hydroxyl radicals (•OH) and sulfate radicals ($SO_4^{\bullet-}$), as well as non-radical species, can be generated from PMS molecules with an asymmetric structure.[4] In comparison to radical-based ROS, $^1O_2$ has emerged as a particularly attractive oxidant in AOPs due to its inherent benefits, including prolonged longevity, broad pH tolerance, robust electrophilicity, and exceptional target specificity.[5]

Defect engineering has proved to be a promising strategy to promote the catalytic efficiency in Fenton-like reactions. Upon oxygen vacancy formation, electrons adjacent to the defect sites undergo delocalization. This critical electronic restructuring process not only significantly enhances surface activation but also concurrently improves the charge transfer capability and electrical conductivity. Consequently, transition metal oxides enriched with oxygen vacancies exhibit exceptional PMS activation efficiency in Fenton-like systems.[6] In a typical example, Zhu *et al.* introduced oxygen vacancies on commercial MnO_2 surfaces under ambient atmospheric conditions. The resulting defect-rich MnO_2 exhibited enhanced catalytic performance in PMS activation, achieving complete mineralization of tetrabromobisphenol (TBBPA) with a remarkable pseudo-first-order rate constant of 0.21 min^{-1}, a notable 22-fold enhancement compared to pristine MnO_2.[7] Although the metal oxide-activated persulfate system exhibited advantageous characteristics such as mild reaction conditions, cost-effectiveness, and high efficiency,[8] they often suffer from the obstacles of agglomeration of the active components, which leads to diminished catalytic efficacy and durability. The integration of carbon-based materials holds promise for bolstering the electron transfer capacity of metal oxide components and establishing robust covalent bonds between carbon carriers and metal elements, ultimately enhancing the stability of catalysts.[9]

Inspired by the preceding discussions, we propose an innovative defect engineering strategy that synergistically integrates bimetallic oxide architecture with oxygen vacancy modulation, yielding a CNFs@$CoMnO_x$-500 catalyst featuring exceptional PMS activation efficiency. The study also delved into the examination of various influential factors, including catalyst and PMS dosage, pH of the solution, co-existing anions, and natural organic matter, among others. Concurrently, the generated ROS species are identified through quenching experiments and electron paramagnetic resonance (EPR) spectroscopy analysis. The findings demonstrate the effectiveness of the CNFs@$CoMnO_x$ catalyst for rhodamine (RhB) degradation *via* non-radical pathways, specifically $^1O_2$ species.

The synthesis procedure and structural evolution of the CNFs@$CoMnO_x$-500 composite are illustrated in Fig. 1, which involves a co-deposition strategy followed by controlled thermal annealing at 500 °C under an inert atmosphere. During the initial deposition process, a critical redox reaction occurs between $KMnO_4$ and carbon that leads to the deposition of MnO_2 nanosheets onto the CNFs ($4MnO_4^- + 3C + H_2O \rightarrow 4MnO_2 +$

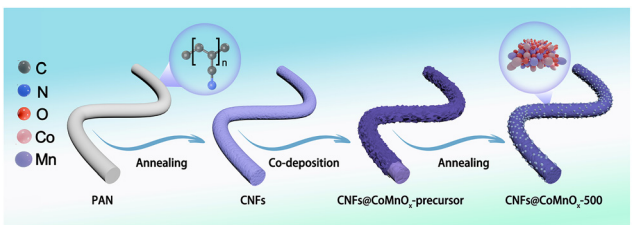

Fig. 1 Schematic diagram for the synthetic process of CNFs@$CoMnO_x$-500 nanofibers.

Alan G. MacDiarmid Institute, College of Chemistry, Jilin University, 2699 Qianjin Street, Changchun 130012, P. R. China. E-mail: xflu@jlu.edu.cn

CO_3^{2-} + $2HCO_3^-$).[10] As depicted in Fig. S1a and b, bare CNFs display smooth surfaces with a uniform nanofibrous morphology, featuring an average diameter of 152 nm. Subsequent precursor integration through sequential treatment with $Co(NO_3)_2$ and $KMnO_4$ solutions induces uniform growth of two-dimensional nanosheet architectures on the surface of the CNFs, resulting in a notable diameter increase to 180 nm (Fig. 2a and Fig. S1c). TEM characterization further confirms the coherent growth of the hierarchical nanostructures, revealing well-defined interfacial contact between the CNF core and the deposited $MnCoO_x$-precursor phases (Fig. S2). Upon annealing at 500 °C, the surface morphology of the CNFs@$CoMnO_x$-precursor undergoes a dramatic transformation from nanosheets to nanoparticles, with the average diameter reduced to 158 nm (Fig. 2b, c and Fig. S1d). Consistent with this observation, Fig. S3–S6 demonstrate that the elevated annealing temperature leads to progressively refined nanoparticle structure of $CoMnO_x$. For comparison, when solely $KMnO_4$ is introduced into the reaction system, thin nanosheets form on the surface of the CNFs (Fig. S7a), which evolve into nanoparticles following low-temperature annealing treatment (Fig. S7b). In contrast, the presence of Co^{2+} alone induces minimal nanosheet deposition on the CNF surface, with negligible morphological alterations observed before and after thermal treatment (Fig. S7c and d). The structural evolution of the catalyst series is analyzed by XRD measurement. As illustrated in Fig. S8, the precursors exhibit amorphous characteristics prior to annealing. Upon annealing at 400 °C, the XRD patterns resolve two distinct crystalline phases: (Co, Mn)(Co, $Mn)_2O_4$ and CoO. On increasing the annealing temperature to 500 °C and 600 °C, the diffraction peaks of the products position between those of CoO (JCPDS # 70-2856) and MnO (JCPDS # 78-0424), with no secondary phases detected (Fig. 2d). This phase progression confirms the formation of a bimetallic $CoMnO_x$ solid solution structure on CNFs.[11] Raman spectroscopy further corroborates the structural evolution of the obtained CNFs@$CoMnO_x$-500. The Mn–O stretching vibration in CNFs@MnO_x-500 appears at 656 cm^{-1}, while in the CNFs@$CoMnO_x$-precursor and CNFs@$CoMnO_x$-500 samples, this band exhibits a marked shift, suggesting the incorporation of Co species into the lattice (Fig. S9).[12] HRTEM analysis further reveals well-defined lattice fringes with measured interplanar spacings of 0.25 nm and 0.22 nm, corresponding to the (111) and (200) crystallographic planes of CNFs@$CoMnO_x$-500, respectively (Fig. 2e and f). Energy-dispersive X-ray (EDX) spectroscopy confirms the coexistence of Co, Mn, O, C, and N elements in the CNFs@$CoMnO_x$-500 sample (Fig. S10), while the elemental mapping demonstrates their spatially homogeneous distribution across the nanostructure (Fig. 2g). EPR analysis reveals that the CNFs@$CoMnO_x$-precursor sample exhibits a characteristic signal at g = 2.003 (Fig. S11a), which is typically associated with unpaired electrons trapped at oxygen vacancies.[13] Complementary XPS deconvolution of the O 1s spectra resolves three distinct contributions, including lattice oxygen (O_{lat}) at 530.2 eV, oxygen vacancies at 531.3 eV, and surface–adsorbed hydroxyl species from H_2O (O_{H_2O}) at 532.2 eV (Fig. S11b).[14] Comparative quantification reveals that both CNFs@$CoMnO_x$-400 (29.7%) and CNFs@$CoMnO_x$-500 (28.4%) exhibit significantly elevated oxygen vacancy fractions relative to CNFs@$CoMnO_x$-600 (21.6%). It can be concluded that the oxygen vacancy concentration decreases in the following order: CNFs@$CoMnO_x$-400 ≈ CNFs@$CoMnO_x$-500 > CNFs@$CoMnO_x$-600. The chemical valence states of various crystalline materials were further investigated by Co 2p and Mn 2p XPS spectra. As illustrated in Fig. S12a, the Mn 2p spectrum exhibits two primary spin–orbit components of Mn $2p_{1/2}$ at 653.4 eV and Mn $2p_{3/2}$ at 642.1 eV, respectively. High-resolution fitting of the Mn $2p_{3/2}$ identifies three distinct oxidation states of Mn^{2+} (641.1 eV), Mn^{3+} (642.5 eV), and Mn^{4+} (644.1 eV).[15] The Co 2p exhibits characteristic peaks at 782.2 eV (Co^{2+} $2p_{3/2}$) and 796.9 eV (Co^{2+} $2p_{1/2}$), with additional features at 780.5 eV (Co^{3+} $2p_{3/2}$) and 795.6 eV (Co^{3+} $2p_{1/2}$), complemented by satellite peaks at 787.5 eV and 801.9 eV (Fig. S12b).[16] It can be seen that as the temperature increases, the oxidation states of Co and Mn decrease.

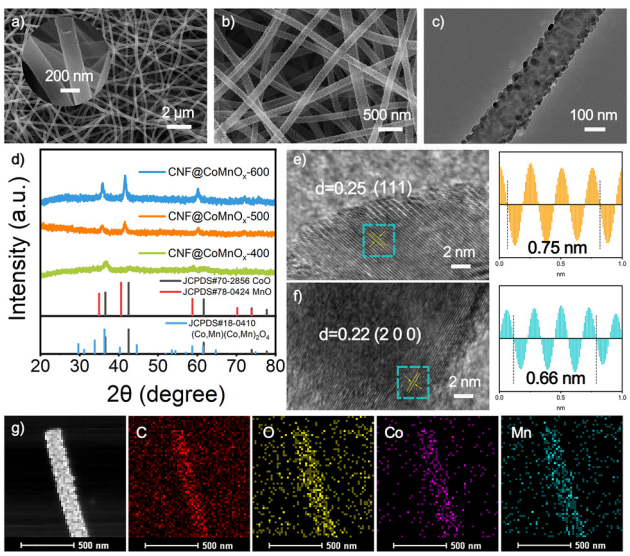

Fig. 2 (a) FESEM image of CNFs@$CoMnO_x$-precursor nanofibers. (b) and (c) FESEM and TEM image; (d) XRD patterns; (e) and (f) HRTEM image; (g) HAADF-STEM and EDX mappings of CNFs@$CoMnO_x$-500.

We systematically investigated the PMS activation capability of CNFs@$CoMnO_x$-500 through RhB degradation, a typical model reaction for AOPs. Control experiments demonstrate negligible RhB degradation (below 5%) with CNFs@$CoMnO_x$-500 alone and <10% with PMS only (Fig. 3a). Strikingly, the first-order kinetic constant (k, min^{-1}) for RhB degradation is substantially enhanced in the CNFs@$CoMnO_x$-precursor/PMS system, reaching a value of 0.249 min^{-1} (Fig. 3b, c and Fig. S13). The favorable catalytic performance of the CNFs@$CoMnO_x$-precursor sample can be attributed to its oxygen vacancies. Notably, after the annealing treatment, the k value of the obtained CNFs@$CoMnO_x$-500 increases to 0.659 min^{-1}. This performance underscores the synergistic interplay between the bimetallic solid solution architecture and oxygen vacancy in modulating redox-active sites. For comparative analysis, the catalytic performances in the monometallic counterparts of CNFs@CoO_x-500 and CNFs@MnO_x-500 are suboptimal, achieving merely 42.0% and 28.7% RhB degradation, respectively (Fig. 3a).

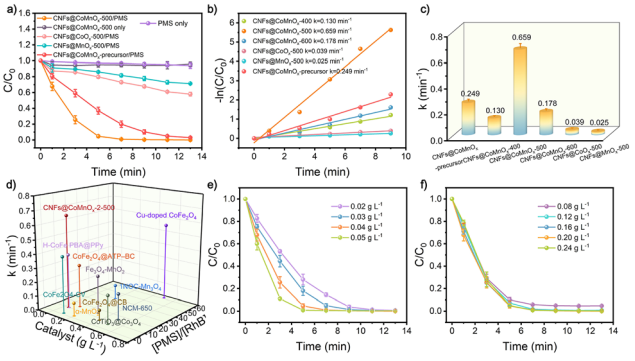

Fig. 3 (a) RhB degradation curves. (b) The corresponding fitted kinetics curves. (c) Histogram of first-order kinetic constant values in varied catalytic reaction systems. (d) Comparison of the intrinsic catalytic activity of the CNFs@CoMnO$_x$-500 with reported catalysts towards PMS activation. Effect of (e) catalyst dosage, and (f) PMS concentration on RhB degradation.

As evidenced in Fig. 3d, the CNFs@CoMnO$_x$-500 catalyst also exhibits exceptional activity, surpassing numerous PMS-activated catalysts reported in the literature and positioning it as a leading candidate for high-efficiency AOPs. Additionally, the impact of catalyst dosage on RhB degradation efficiency is systematically evaluated (Fig. 3e). The results reveal that increasing the catalyst dosage from 0.02 to 0.04 g L^{-1} enhances the RhB degradation rate from 0.345 min^{-1} to 0.659 min^{-1}. Balancing catalytic efficacy with cost considerations, 0.04 g L^{-1} is identified as the optimal dosage for subsequent studies. Further investigation of PMS dosage effects (Fig. 3f) demonstrates a proportional improvement in RhB degradation kinetics within 0.08–0.20 g L^{-1}. However, when the PMS dosage reaches 0.24 g L^{-1}, a notable decline in degradation efficiency is observed, which is likely due to the PMS-PMS interactions producing less reactive species.[17] Consequently, 0.20 g L^{-1} PMS is selected as the benchmark concentration to maximize oxidative radical utilization. The catalytic degradation rate exhibits a pronounced temperature dependence, increasing markedly with rising temperature (Fig. S14).[18] Systematic evaluation across pH 3.0–11.0 reveals the broad operational versatility of the CNFs@CoMnO$_x$-500 catalyst, achieving complete RhB elimination at pH 5.0–9.0, whereas the degradation efficiency declines to 79.2% at pH 3.0 and 51.1% at pH 11.0 (Fig. S15a and b). As illustrated in Fig. S16, HCO_3^- notably suppresses RhB degradation in the CNFs@CoMnO$_x$-500/PMS system. This decrease stems from the fact that HCO_3^- scavenges reactive radicals ($^{\bullet}SO_4^-$, $^{\bullet}OH$) to generate less oxidative $CO_3^{\bullet-}$, while simultaneously elevating the solution pH to shift PMS speciation toward less reactive SO_5^{2-}.[19] Notably, the RhB efficiency remains robust against most of the common anions and even humic acid, demonstrating remarkable tolerance to treat complex water. As shown in Fig. S17, the CNFs@CoMnO$_x$-500 catalyst demonstrates superior degradation performance across all tested dyes, yet exhibits marginally reduced efficacy toward the antibiotic levofloxacin (LEVO). The slightly reduced degradation efficiency of CNFs@CoMnO$_x$-500 for RhB in complex aqueous environments can be attributed to its interference with co-existing ions (Fig. S18). The operational stability is rigorously assessed, revealing that the CNFs@CoMnO$_x$-500 catalyst maintains 97.1% RhB removal efficiency after five successive cycles, confirming its exceptional recyclability (Fig. S19). Post-catalysis characterization through XRD, SEM, and TEM analysis reveals the retention of structural integrity, with well-preserved crystallographic features and morphological stability (Fig. S20). Its practical implementation potential is evaluated in a membrane-based water purification platform (Fig. S21). Composite membranes are engineered *via* vacuum–assisted filtration of CNFs@CoMnO$_x$-500 suspensions onto polyvinylidene fluoride (PVDF) supports.[20] Performance analysis demonstrates that the pristine PVDF membrane displays limited initial RhB adsorption capacity and almost negligible adsorption after 140 min. In contrast, under continuous operation, the functionalized membrane with the catalyst achieves a sustained RhB degradation efficiency of 97.6%.

To identify the ROS involved in RhB degradation mediated by the CNFs@CoMnO$_x$-500 catalyst, quenching experiments are systematically conducted. EtOH is recognized as an effective scavenger for both $^{\bullet}OH$ and $SO_4^{\bullet-}$,[21] while TBA is a selective scavenger for $^{\bullet}OH$, which are employed to assess radical contributions.[22] As depicted in Fig. 4a and Fig. S22, both $SO_4^{\bullet-}$ and $^{\bullet}OH$ scavengers demonstrate negligible inhibitory effects on the CNFs@CoMnO$_x$-500/PMS system, with the degradation efficiency remaining largely unaffected even at elevated concentrations (200–400 mM). This finding suggests limited involvement of free $SO_4^{\bullet-}$ and $^{\bullet}OH$ in the catalytic process. Complementary experiments with 10 mM FFA,[23,24] demonstrate a significant 18.3% decrease in RhB removal efficiency, confirming the substantial involvement of $^1O_2$ in the catalytic mechanism. Further investigation into $^1O_2$ generation within the CNFs@CoMnO$_x$-500/PMS system is conducted to unravel the mechanistic pathways. The dependence on the dissolved oxygen is rigorously evaluated by purging the reaction medium with argon (Ar) for 30 min prior to catalytic activation. Notably, dissolved oxygen removal *via* Ar purging induces only minor slowdown in the RhB degradation rate (Fig. S23). These observations conclusively exclude molecular oxygen as the predominant $^1O_2$ precursor in this catalytic system.[25] EPR spectroscopy is further employed to identify ROS generated during PMS activation. Systematic spin-trapping experiments using DMPO for radical species detection (*e.g.*, $^{\bullet}OH$ and $SO_4^{\bullet-}$) and TEMP for $^1O_2$ identification reveal diagnostic spectral signatures.[26]

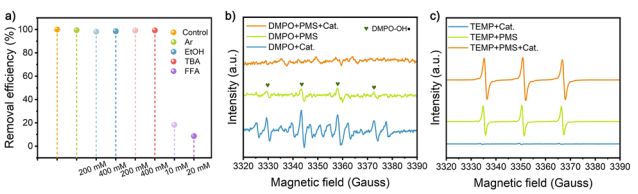

Fig. 4 (a) The quenching tests of the CNFs@CoMnO$_x$-500/PMS system with diverse quenching agents. EPR spectra for (b) DMPO–$^{\bullet}OH$ and (c) TEMP–$^1O_2$.

The DMPO–PMS system exhibits characteristic 1 : 2 : 2 : 1 quadruplet signals, corresponding to DMPO–$^{\bullet}$OH adducts (Fig. 4b). Remarkably, the introduction of CNFs@CoMnO$_x$-500 into the DMPO–PMS system markedly attenuates these signals to near-background levels. In contrast, a prominent 1 : 1 : 1 triplet signal emerges in the TEMP–PMS system and an enhancement after the addition of the CNFs@CoMnO$_x$-500 catalyst, providing unequivocal evidence of $^1O_2$ generation (Fig. 4c). Control experiments reveal diminished $^1O_2$ signals in the catalyst-only system, demonstrating that $^1O_2$ serves as the predominant reactive species governing RhB degradation in the CNFs@CoMnO$_x$-500/PMS system.

XPS analysis is used to elucidate the catalytic mechanism of the CNFs@CoMnO$_x$-500/PMS system. As illustrated in Fig. S24a, quantitative deconvolution reveals a discernible decrease in the Co^{2+} contribution from 39.4% to 37.2%, accompanied by a proportional increase in Co^{3+} content from 60.6% to 62.8% after the catalytic degradation reaction. This redox evolution indicates electron transfer from Co^{2+} to PMS during activation, with subsequent regeneration of Co^{2+} *via* reduction of Co^{3+} by HSO_5^- and the SO_4^{2-} intermediate, thereby generating reactive $SO_5^{\bullet-}$ and OH$^{\bullet}$ species.[27] For Mn species, quantitative XPS analysis reveals a notable valence state redistribution, indicating an Mn-mediated electron redistribution process (Fig. S24b). Parallel characterization from XPS and EPR spectroscopy demonstrates a marked reduction in oxygen vacancy content from 28.4% to 19.7% after the catalytic degradation reaction (Fig. S24c and S25), confirming the pivotal role of these structural defects in electron transfer mechanisms during redox cycling. Additionally, oxygen vacancies operate as PMS adsorption sites, facilitating electron transfer to surface-bound PMS, which increases the production of ROS.[28]

The degradation mechanism of RhB is systematically elucidated by high-performance liquid chromatography mass spectrometer (HPLC-MS) measurement.[29] The primary degradation pathway initiates with sequential *N*-deethylation, consistent with the established literature,[30] wherein RhB (m/z = 443) undergoes stepwise ethyl group elimination to yield P1 (m/z = 415) and P2 (m/z = 331) (Fig. S26 and S27). Subsequently, cleavage induces chromophore destruction *via* dehydroxylation of the product to produce P3, P4 and P5. Progressive fragmentation of these aromatic intermediates through bond scission and oxidation ultimately produces low-molecular-weight aliphatic compounds (P6–P8).

In this study, an oxygen vacancy-enriched CNFs@CoMnO$_x$-500 catalyst is strategically prepared *via* a co-precipitation protocol coupled with an annealing process. The catalyst exhibits exceptional PMS activation capability, achieving an impressive over 99% RhB degradation within 13 min. Mechanistic studies identify $^1O_2$ as the dominant ROS, with the oxygen vacancy-abundant interface facilitating PMS adsorption and electron shuttling. This work establishes a paradigm for designing multifunctional composite catalysts, offering critical guidelines for optimizing AOPs.

Siyu Ren: investigation, data curation and drafting the manuscript. Yue Zhang: investigation. Linfeng Zhang: investigation. Xiaofeng Lu: funding acquisition, resources, review and editing and supervision.

Conflicts of interest

There are no conflicts to declare.

Data availability

The data supporting this article have been included as part of the supplementary information (SI). Supplementary information: detailed experimental procedures, supplementary figures, and tables. See DOI: https://doi.org/10.1039/d5cc06807j.

Acknowledgements

This work was financially supported by the National Natural Science Foundation of China (52273056).

References

1 Y. Wang, M. Zhong, F. Ma, C. Wang and X. Lu, *Water Res.*, 2025, **268**, 122655.
2 H. Liu, X. Shu, M. Huang, B. Wu, J. Chen, X. Wang, H. Li and H. Yu, *Nat. Commun.*, 2024, **15**, 2327.
3 N. Song, S. Ren, Y. Zhang, C. Wang and X. Lu, *Adv. Funct. Mater.*, 2022, **32**, 2204751.
4 G. Bi, R. Ding, J. Song, M. Luo, H. Zhang, M. Liu, D. Huang and Y. Mu, *Angew. Chem., Int. Ed.*, 2024, **63**, e202401551.
5 Z. Wang, E. Almatrafi, H. Wang, H. Qin, W. Wang, L. Du, S. Chen, G. Zeng and P. Xu, *Angew. Chem., Int. Ed.*, 2022, **61**, e202202338.
6 P. Muhammad, A. Zada, J. Rashid, S. Hanif, Y. Gao, C. Li, Y. Li, K. Fan and Y. Wang, *Adv. Funct. Mater.*, 2024, **34**, 2314686.
7 S. Ndayiragije, Y. Zhang, Y. Zhou, Z. Song, N. Wang, T. Majima and L. Zhu, *Appl. Catal., B*, 2022, **307**, 121168.
8 B. Li, Y. Liu, K. Hu, Q. Dai, C. Chen, X. Duan, S. Wang and Y. Wang, *Adv. Funct. Mater.*, 2024, 2401397.
9 Y. Long, P. Yang, C. Wang, W. Wu, X. Chen, W. Liu, Z. Cao, X. Zhan, D. Liu and W. Huang, *Chem. Eng. J.*, 2023, **456**, 140996.
10 G. Nie, Z. Zhang, Y. Liu, J. Wang, C. Fu, H. Yin, J. Chen, L. Zhao and Z. Pan, *Adv. Fiber Mater.*, 2022, **4**, 1129–1140.
11 X. Yu, R. Qi, L. Zhang, L. Deng, M. Zhong, Z. Chen and X. Lu, *Acta Mater.*, 2025, **294**, 121165.
12 L. Song, H. Zhang, J. Xiong, Z. Chen, Y. Liu, H. Zhou, W. Yang, D. Cao, H. Huang, L. Chen, M. Fu and D. Ye, *Appl. Catal., B*, 2024, **343**, 123547.
13 S. Qiao, Q. Wang, D. Lei, X. Shi, Q. Zhang, C. Huang, A. Liu, G. He and F. Zhang, *J. Mater. Chem. A*, 2022, **10**, 11702.
14 L. Liu, Y. Tang, S. Liu, M. Yu, Y. Sun, X. Fu, J. Luo and S. Liu, *Adv. Energy Mater.*, 2025, **15**, 2402967.
15 N. Luo, F. Gao, H. Liu, T. Xiong, J. Wen, E. Duan, C. Wang, S. Zhao, H. Yi and X. Tang, *Appl. Catal., B*, 2024, **343**, 123442.
16 S. Lee, S. W. Byun, S. Kweon, H. Shin, H. K. Min, M. B. Park and S. B. Kang, *Appl. Catal., B*, 2024, **340**, 123264.
17 H. Xiao, Y. Wang, K. Lv, C. Zhu, X. Guan, B. Xie, X. Zou, X. Luo and Y. Zhou, *Water Res.*, 2025, **278**, 123399.
18 R. Wu, X. Hu, Y. Li, Y. Li, Y. Cai, P. Jiang and B. Yu, *Chem. Eng. J.*, 2023, **473**, 145011.
19 S. Ren, N. Song, Y. Zhang, C. Wang and X. Lu, *Appl. Surf. Sci.*, 2024, **674**, 160965.
20 P. Wang, Z. Zhao, L. Zhang, S. Zhan and Y. Li, *Adv. Funct. Mater.*, 2024, **34**, 2316542.
21 Y. He, H. Qin, Z. Wang, H. Wang, Y. Zhu, C. Zhou, Y. Zeng, Y. Li, P. Xu and G. Zeng, *Appl. Catal., B*, 2024, **340**, 123204.
22 Z. Yao, Y. Chen, X. Wang, K. Hu, S. Ren, J. Zhang, Z. Song and N. Ren, *Nat. Commun.*, 2025, **16**, 148.

23 F. Li, Z. Wan, D. Zheng, L. Zhang, W. Huang, F. Chen, J. Deng, Z. Qi, G. Li and F. Zhang, *Chem. Eng. J.*, 2024, **482**, 149052.
24 D. Qi, J. Wang, J. Zhang, K. Su, J. Xu, W. Lv, Y. Wang, Z. Zhang and Y. Xiao, *Adv. Funct. Mater.*, 2024, 2406470.
25 J. Pei, J. Liu, K. Fu, Y. Fu, K. Yin, S. Luo, D. Yu, M. Xing and J. Luo, *Nat. Commun.*, 2025, **16**, 800.
26 Z. Zhang, P. Duan, J. Zheng, Y. Xie, C. Bai, Y. Sun, X. Chen, F. Chen and H. Yu, *Nat. Commun.*, 2025, **16**, 115.
27 J. Xu, Y. Wang, J. Wan and L. Wang, *Sep. Purif. Technol.*, 2022, **287**, 120576.
28 X. Li, L. Li, J. Wang, H. Guo, Y. Sun, Z. Zhang, F. Yang and Y. Ding, *Chem. Eng. J.*, 2025, **526**, 171318.
29 S. Ren, L. Zhang, Y. Zhang, C. Wang and X. Lu, *Inorg. Chem.*, 2025, **64**, 8064–8073.
30 W. Li, Y. Zhang, P. Zhao, P. Zhou, Y. Liu, X. Cheng, J. Wang, B. Yang and H. Guo, *J. Hazard. Mater.*, 2020, **393**, 122399.